



Neutron Diffraction Magnetic and Mossbauer Spectroscopic Studies of $\text{Pb}_{0.8}\text{Bi}_{0.2}\text{Fe}_{0.728}\text{W}_{0.264}\text{O}_3$ and $\text{Pb}_{0.7}\text{Bi}_{0.3}\text{Fe}_{0.762}\text{W}_{0.231}\text{O}_3$ Ceramics

I. Shivaraja¹ · Shidaling Matteppanavar² · P. S. R. Krishna³ · Sudhindra Rayaprol⁴ · P. D. Babu⁴ · V. Jagadeesha Angadi⁵ · S. P. Kubrin⁶ · Basavaraj Angadi¹

Received: 15 November 2020 / Accepted: 5 January 2021 / Published online: 16 January 2021
© The Author(s), under exclusive licence to Springer Science+Business Media, LLC part of Springer Nature 2021

Abstract

We report on high-temperature crystallographic structure, magnetic and physical properties of chemically B-site disordered lead-bismuth iron tungstate, $(\text{PFW})_{1-x}(\text{BFO})_x$ (which can be written as $\text{Pb}_{0.8}\text{Bi}_{0.2}\text{Fe}_{0.728}\text{W}_{0.264}\text{O}_3$ (0.8PFW–0.2BFO) for $x = 0.2$ and $\text{Pb}_{0.7}\text{Bi}_{0.3}\text{Fe}_{0.762}\text{W}_{0.231}\text{O}_3$ (0.7PFW–0.3BFO) for $x = 0.3$) or PBFW, solid solutions through neutron diffraction (ND), magnetization, electron paramagnetic resonance, and Mössbauer spectroscopic studies. From the high temperature magnetic susceptibility measurement, it is observed that increase antiferromagnetic to paramagnetic phase transition around $T_N = 435$ K ($\text{Pb}_{0.8}\text{Bi}_{0.2}\text{Fe}_{0.728}\text{W}_{0.264}\text{O}_3$) and 504 K ($\text{Pb}_{0.7}\text{Bi}_{0.3}\text{Fe}_{0.762}\text{W}_{0.231}\text{O}_3$), compared to pure PFW. Room-temperature crystallographic study confirms the formation of pseudo *cubic* structure with *Pm-3m* space group, whereas the magnetic structure is commensurate G-type antiferromagnetic ordering. The obtained temperature dependent structural parameters from the ND, evidenced to existence of strong spin-lattice coupling around T_N for both the compounds. The discontinuity in the Pb/Bi–O bond length around ferroelectric transition (T_C) indicates the presence of magnetoelectric coupling. Interestingly, microscopic 1:1 B-site ordered nanoclusters of PBFW exhibits the ferrimagnetic clusters along with antiferromagnetic order and it observed through the opening of M vs H hysteresis curves in the lower field regime. The EPR and Mössbauer spectroscopic studies well support the magnetic property and also reveal the Fe^{+3} state, and the weak signal in EPR and broader linewidth in the Mössbauer spectra exhibit the B-site disorderliness.

Keywords Spin lattice · Magnetoelectric coupling · Neutron diffraction · Ferrimagnetism and antiferromagnetism

1 Introduction

Recently, multiferroic materials have gained enormous attention due to the coupling of spin, charge, and lattice degrees of

freedom in single-phase materials [1, 2]. This coupling between these three ferroic properties leads to the realization of technologically potential device applications such as magnetoelectric memory, voltage tunable spintronics, transducers, and sensors [3–7]. In this context, the coupling mechanisms in such single-phase materials need a proper understanding of the underlying fundamental physical concepts, attracting many researchers in solid-state and materials science. Due to the symmetry constraints such as magnetic symmetries, time-reversal, and spatial inversion symmetry, only a few multiferroic materials occur naturally [8]. Due to the contradictory nature in the origin of magnetism by d^n (n indicates the free/unpaired electrons in transition $3d$ elements) while ferroelectricity from d^0 , it is difficult to obtain the multiferroic properties in the ABO_3 (A: Pb, Bi, Sc, and Ba, etc.; and B: transition metal ions Fe, Co, Ni, Mg, Nb, and W, etc.) perovskites. Free electrons in the d shell suppress the ferroelectricity in a simple ABO_3 structure [8, 9]. Therefore, to overcome from these issues, the complex perovskite system with structure

✉ Basavaraj Angadi
brangadi@gmail.com

¹ Department of Physics, Bangalore University, Jnanabharathi Campus, Bangalore 560 056, India

² Department of Physics, Basavaprabhu Kore, Arts Science and Commerce College, Chikodi 59120, India

³ Solid State Physics Division, BARC, Mumbai 400085, India

⁴ UGC-DAE-Consortium for Scientific Research, Mumbai Centre, BARC Campus, Mumbai 400085, India

⁵ Department of Physics, P.C. Jabin Science College, Hubballi 31, India

⁶ Research institute of physics, Southern Federal University, Stachkiav.194, Rostov-on-Don, Russia 344090

$A(B'B'')O_3$ are considered, where different source B' and B'' produces the magnetism and ferroelectricity, respectively. A large number of Pb-based systems with $A(B'B'')O_3$ structure and with multiferroic properties such as $Pb(Fe_{1/2}Nb_{1/2})O_3$ (PFN), $Pb(Fe_{1/2}Ta_{1/2})O_3$ (PFT), and $Pb(Fe_{2/3}W_{1/3})O_3$ (PFW) have been reported [10–12]. The PFW and its solid solutions have shown promising multiferroic properties, and PFW has magnetic and ferroelectric transition temperatures at 350 K (T_N) and 150 K (T_C), respectively. It also has some drawbacks like difficulty in synthesizing the single-phase material due to the volatile nature of PbO, lower magnetic moment due to the G-type antiferromagnetic structure, and lower ferroelectric Curie temperature ($T_C = 150$ K) [13–16]. Besides, $Pb(Fe_{2/3}W_{1/3})O_3$ exhibits relaxor behavior in its ferroelectric properties with a 2:1 ratio of Fe and W ions distributed randomly in the octahedral B-site [17, 18]. It should be noted that the random distribution of Fe and W in the B-site of PFW induces the short-range 1:1 (Fe:W) structural ordered region of 3–5 nm [19, 20]. A similar behavior was observed in other compounds such as $Pb(Mg_{1/3}Nb_{2/3})O_3$, $Sr(Fe_{2/3}W_{1/3})O_3$, and

$Ba(Fe_{2/3}W_{1/3})O_3$ [21, 22]. Ivanov et al demonstrated the ferrimagnetic nature in the Sc-doped PFW and $(1-x)(0.79PbFe_{2/3}W_{1/3}O_3-0.21PbSc_{2/3}W_{1/3}O_3)-(x)BiFeO_3$ (PFSW-BFO) solid solution [23]. These materials exhibit B-site 1:1 long-range order leading to the ferrimagnetic nature of a larger spontaneous magnetic moment without affecting the relaxor ferroelectric nature [23–25]. However, the Sc-doped PFW shows the weak chemical cation ordering of about a <5-nm range as nanodomains exhibiting the uncompensated ferrimagnetic moment [23]. The magnetic moment was larger than the disordered simple perovskites and $Bi(Fe_{1/2}Cr_{1/2})O_3$ epitaxial thin film [26]. Recently, Yb- and Sc-doped $Pb(Fe_{2/3}W_{1/3})O_3$ [23, 27] also exhibited similar property. Due to the larger ionic radii of the Yb and Sc, compared to Fe, they form the alternative Fe and Yb/Sc unit cells up to a few nanometers, which leads to the change of the number of magnetic ions in the neighboring unit cells.

In this regard, from the past few decades, there have been many attempts to improve the multiferroic properties of PFW

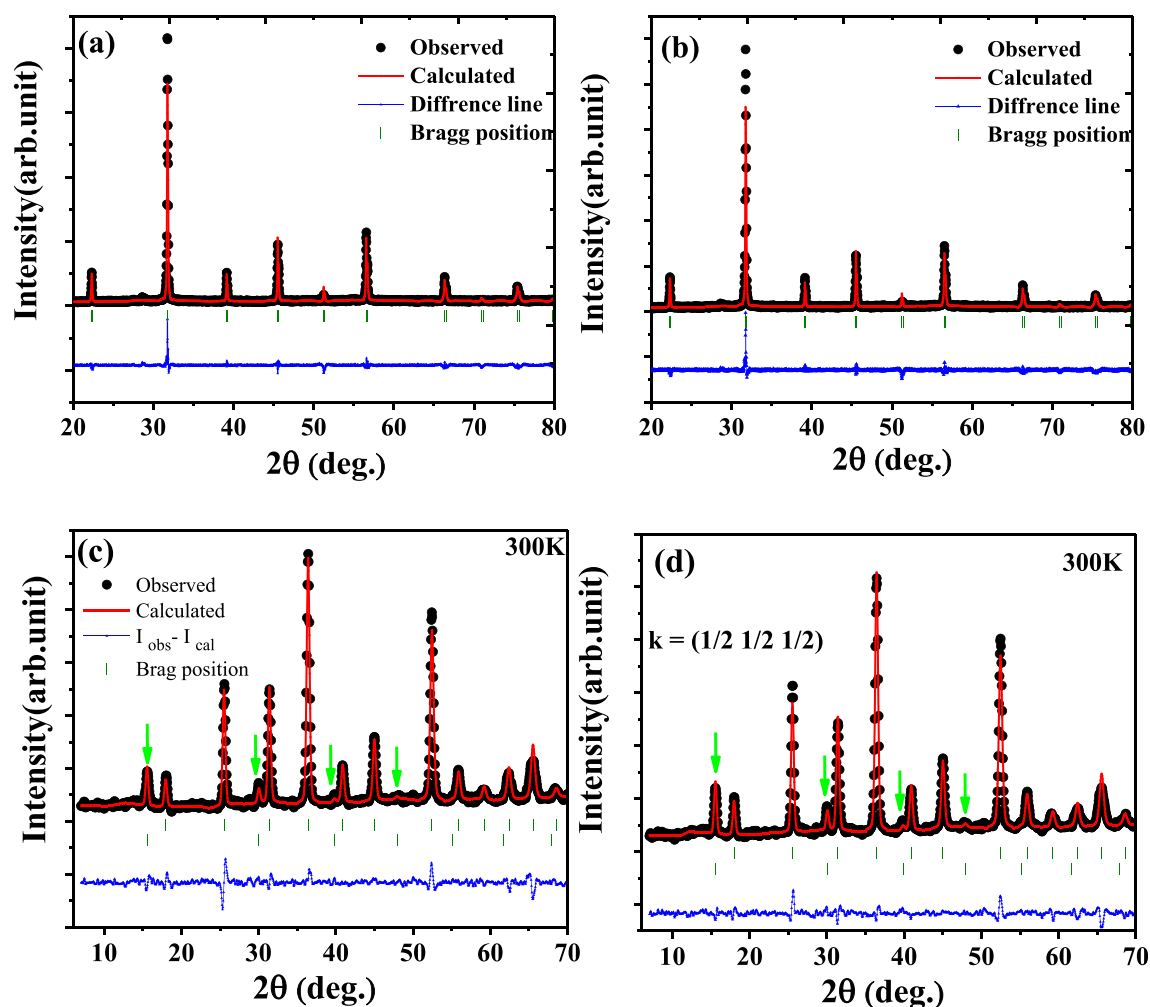


Fig. 1 RT XRD (a, b) and NPD (c, d) Rietveld refined patterns of $(PFW)_{1-x}(BFO)_x$ ($x = 0.2$ and 0.3) and downward arrow mark represents the magnetic Bragg reflections

by substituting or by making solid solutions with PFN, PbTiO_3 , etc. [28–43]. However, by making these solid solutions and substitutions, there were new difficulties like inducing the space charges, and reducing the T_N below the RT, and it rendered to normal ferroelectric behavior. To overcome these problems in PFW and to achieve the RT and above RT multiferroics, we made solid solutions with the well-known RT multiferroic BiFeO_3 (BFO). The BFO has a larger value of ferroelectric and magnetic transition temperature $T_C = 1103$ K and $T_N = 643$ K [44, 45]. In addition, BFO exhibits the G-type antiferromagnetic ordering with the spiral spin structure of spin wavelength ≈ 62 nm. Hence, it exhibits a lower total effective magnetic moment. Recently, BFO doped with Tb^{3+} rare earth showed spatially destructed and the canted G-type spin structure with net magnetic moment [46, 47]. BFO also suffers some difficulties in the high-temperature manufacturing process due to its highly volatile nature [48].

In this work, we synthesized the solid solution of $(\text{PFW})_{1-x}(\text{BFO})_x$ ($x = 0.2$ and 0.3) by columbite method. Crystallographic studies were carried out through XRD and NPD. The temperature-dependent NPD reveals the presence of spin-lattice and magnetoelectric coupling. Also, we successfully achieve the RT magnetoelectric $(\text{PFW})_{1-x}(\text{BFO})_x$ materials. Astonishingly, the magnetization measurement (ZFC and FC) and M vs H curves shows the ferrimagnetic kind of nature along with the antiferromagnetism. The $(\text{PFW})_{1-x}(\text{BFO})_x$ exhibits the G-type antiferromagnetic structure with residual magnetic moment due to the Fe–O–Fe superexchange interaction and anisotropic magnetic nature. The electron paramagnetic resonance (EPR) and Mössbauer studies confirm the oxidation state of Fe at +3 and exhibit the random distribution in the B-site ions.

2 Experiment

The PFBW ceramic samples were synthesized by the two-step solid-state reaction method or Columbite method. The synthesis conditions are reported elsewhere [49]. This method involves two-step calcination processes; in the first step, the stoichiometric amount of starting materials were well-grinded in the ethanol medium for 2 h and calcined at 1000 °C for 4 h, and then calcined at 850 °C for 2 h in the second step. After making the pellets of 1-mm thickness and 8-mm diameter using a hydraulic press (3–5 Ton pressure), they were sintered at 850 °C for 1 h in the Pb- and Bi-rich environment in order to maintain the stoichiometry of the solid solutions [49]. The dense sintered pellets were subjected to room temperature X-ray diffraction (XRD) studies to find the phase purity from 20 to 80 degrees of 2θ range with the 0.01° step size and $1^\circ/\text{min}$ scan speed using Rigaku Ultima IV X-ray diffractometer

Table 1 Rietveld refinement parameters of the RT XRD pattern for $(\text{PFW})_{1-x}(\text{BFO})_x$ solid solutions

Structural model	Composition	
	$x=0.2$	$x=0.3$
$a=b=c$ (Å)	3.9825(7)	3.9833(5)
Volume (Å ³)	63.168	63.204
Pb/Bi		
X	0.0000	0.0000
Y	0.0000	0.0000
Z	0.0000	0.0000
Fe/W		
X	0.5000	0.5000
Y	0.5000	0.5000
Z	0.5000	0.5000
O		
X	0.5000	0.5000
Y	0.5000	0.5000
Z	0.0000	0.0000
Bond length (Å)		
Pb/Bi–O	2.8161 (6)	2.8166 (5)
Fe/W–O	1.9912 (5)	1.9916 (5)
Density (g/cm ³)		
Theoretical	9.075	8.963
Experimental	8.184	7.690
χ^2	11.53	8.38
R_{wp}	20.1	21.7
R_p	16.0	18.4

($\lambda = 1.5405$ Å, Japan made). The temperature-dependent Neutron powder diffraction was carried in the temperature range from 300 to 523 K and 300 to 623 K for $x = 0.2$ and 0.3 compositions, respectively. The powder samples were placed in the vanadium can, and the data was collected in the 2θ range of 7 – 135° with the step size of 0.05° using the wavelength of $\lambda = 1.244$ Å on PD-2 powder diffractometer [50] and experiment was carried out at the Dhruva reactor, Trombay Mumbai. The whole XRD and NPD data were analyzed through the Rietveld refinement using Fullprof suite software [51]. The surface morphological studies were carried out by scanning electron microscopy (SEM, JEOL, JSM Japan). The Raman spectroscopic studies were carried out at RT using a 785-nm excitation source (Micro Raman (HORIBA), 100 mW power LASER). Temperature evolution of DC-magnetic susceptibility (χ vs T) was studied with zero (ZFC) and 500 Oe field (FC) in the temperature range 300 – 800 K, and magnetic moment variation with an applied field (M vs H) was studied at the selected temperature of 300 , 450 , and 600 K, by using vibrating sample magnetometer (VSM,

Table 2 Structural parameters and conventional reliability indices obtained from Rietveld refinement of NPD data (PFW)_{1-x}(BFO)_x solid solution ($x = 0.2$) at different temperatures

Composition $x=0.2$								
Temperature (K)	300	313	353	403	433	453	473	523
Lattice parameter (Å)								
a=b=c	3.9796 (1)	3.9795 (1)	3.9818 (1)	3.9843 (1)	3.9857 (1)	3.9867 (1)	3.9906 (1)	3.9933 (1)
Magnetic moment μ_B	1.40 (2)	1.56 (3)	1.24 (2)	0.81 (3)	0.63 (3)	0.40 (5)	–	–
Bond length (Å)								
Pb/Bi–O	2.8140 (8)	2.8139 (12)	2.8156 (9)	2.8173 (8)	2.8183 (9)	2.8190 (9)	2.8218 (9)	2.8237 (9)
Fe/W–O	1.9898 (6)	1.9897 (9)	1.9909 (6)	1.9921 (6)	1.9929 (6)	1.9933 (6)	1.9953 (6)	1.9966 (6)
χ^2	9.21	19.84	9.01	8.05	8.31	8.69	8.06	7.78
R_{wp}	22.7	33.0	23.0	22.7	23.4	24.3	22.5	22.5
R_{mag} -Factor	19.6	24.5	14.5	30.2	50.2	47.2	–	–
B_{iso} (Å ²)								
Pb/Bi	4.145 (4)	3.669 (2)	3.984 (4)	3.917 (9)	4.120 (1)	4.210 (1)	4.246 (9)	4.373 (4)
Fe/W	0.284 (1)	0.034 (6)	0.208 (1)	0.348 (2)	0.349 (2)	0.452 (1)	0.371 (5)	0.522 (2)
O	1.265 (2)	0.888 (5)	1.199 (1)	1.393 (9)	1.433 (2)	1.555 (2)	1.580 (4)	1.655 (2)

oscillation frequency/amplitude 40 Hz /2 mm, 0–9 T field, USA). The magnetic resonance studies were carried out through the electron paramagnetic resonance spectra (EPR) at selected temperatures of 300, 373, and 473 K in the X-Band frequency range (8.75–9.65 GHz, JEA-FA200). The Mössbauer spectra were studied by using MS1104Em spectrometer with a constant acceleration mode. The moving-source geometry was employed. The γ -ray source was ⁵⁷Co in a Rh matrix. The isomer shifts were calculated with respect to the metallic α -Fe. The experimental spectra were fitted using SpectrRelax software [52].

3 Results and Discussion

3.1 Structural Studies

3.1.1 Room Temperature X-Ray and Neutron Powder Diffraction

Figure 1a and b depict the room temperature (RT) Rietveld refined X-ray diffraction pattern of (PFW)_{1-x}(BFO)_x ($x = 0.2$ and 0.3) solid solutions. It can be seen from the figure that the synthesized material is in pure form without any secondary phases, and by comparing with the standard JCPDS pattern

Table 3 Structural parameters and conventional reliability indices obtained from Rietveld refinement of NPD data (PFW)_{1-x}(BFO)_x solid solution ($x = 0.3$) at different temperatures

Composition $x=0.3$											
Temperature (K)	300	333	353	373	383	433	473	533	553	573	623
Lattice parameter(Å)											
a=b=c	3.977 2(1)	3.9785 (1)	3.9794 (1)	3.9804 (1)	3.9813 (1)	3.9837 (1)	3.9859 (1)	3.9910 (1)	3.9920 (1)	3.9929 (1)	3.9957 (1)
Magnetic moment μ_B	1.55 (1)	1.50 (1)	1.38 (1)	1.28 (1)	1.17 (1)	0.85 (2)	0.47 (3)	–	–	–	–
Bond length (Å)											
Pb/Bi–O	2.8123 (7)	2.8132 (7)	2.8138 (7)	2.8145 (7)	2.8152 (7)	2.8169 (7)	2.8184 (7)	2.8220 (7)	2.8227 (7)	2.8234 (7)	2.8254 (7)
Fe/W–O	1.9886 (5)	1.9892 (5)	1.9897 (5)	1.9902 (5)	1.9906 (5)	1.9918 (5)	1.9929 (5)	1.9955 (5)	1.9960 (7)	1.9964 (5)	1.9978 (5)
χ^2	5.87	5.38	5.00	4.97	4.91	4.33	4.30	3.99	4.25	4.31	4.14
R_{wp}	17.9	17.2	16.9	17.1	17.0	16.5	16.9	15.8	16.6	16.8	16.8
R_{mag} -Factor	12.6	10.8	13.8	12.9	15.4	31.3	56.1	–	–	–	–
B_{iso} (Å ²)											
Pb/Bi	4.654 (1)	4.550 (1)	4.661 (6)	4.753 (9)	4.620 (1)	4.805 (1)	4.905 (8)	5.005 (1)	4.962 (3)	5.045 (1)	5.206 (1)
Fe/W	0.136 (0)	0.170 (8)	0.207 (5)	0.279 (2)	0.227 (4)	0.341 (9)	0.474 (7)	0.601 (2)	0.615 (1)	0.720 (1)	0.788 (6)
O	1.704 (1)	1.692 (4)	1.745 (3)	1.775 (7)	1.840 (1)	1.942 (1)	2.095 (1)	2.204 (7)	2.297 (3)	2.271 (8)	2.546 (6)

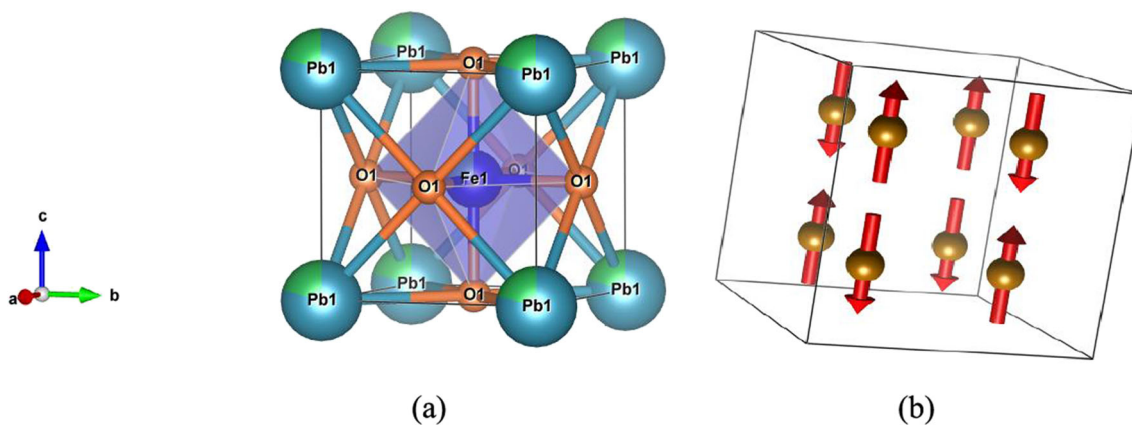


Fig. 2 (a) Polyhedral view and (b) antiferromagnetic spin structure of the $(\text{PFW})_{1-x}(\text{BFO})_x$ ($x = 0.2$ and 0.3) at 300 K

(card no. 89-3132), all peaks are well indexed to the host composition PFW. The obtained reflections are well-matched with the pseudocubic crystal system of space group $Pm-3m$ and confirmed through the Rietveld refinement using the Fullprof suite software [53]. The Pseudo-Voigt function and linear background were used to simulate the peak shape and background of the experimental data respectively. The refined parameters are listed in Table 1. The obtained lattice parameters are decreasing as growing x due to the lower ionic radius of Bi^{3+} ion relative to Pb^{2+} and also consistent with the previous results [54, 55]. The density value obtained in the refinement shows that the synthesized materials are well dense and are nearly 90% and 86% experimental density compared to theoretical ones for $x = 0.2$ and 0.3 , respectively. Figure 1a and b also presented the simulated curve and was well fitted with the experimental data confirmed by observing the χ^2 , R_w , and R_{wp} , etc. In order to have a detailed understanding of the crystal and magnetic structure of PBFW solid solutions, the RT NPD was carried out, as depicted in Fig. 1c and d. The NPD pattern exhibits diffracted reflections related to both crystal or nuclear and magnetic structure which are not coinciding with each other. The green downward arrow marks in Fig. 1c and d represent the magnetic peaks along with other peaks related to the perovskite nuclear structure. In this section, we are discussing only the nuclear structure of the materials, and the magnetic structure will be discussed in the following section. The nuclear structure of the RT NPD data was refined using the FullProf Suite software [51] by considering the pseudocubic crystal symmetry of $Pm-3m$ space group with lattice parameters and atomic positions obtained from the refinement of RT XRD as listed in Table 1. It is worthy of mentioning that the Wyckoff positions of two B-site cations (Fe and W) are in the same $1b$ position at $(\frac{1}{2} \frac{1}{2} \frac{1}{2})$, A site cations (Pb and Bi) at $1a$ position (000) , and O atom at $3c$ position $(\frac{1}{2} \frac{1}{2} 0)$. In order to fit the magnetic peaks, the magnetic propagation wave vector $k = (\frac{1}{2} \frac{1}{2} \frac{1}{2})$ and G-type antiferromagnetic order referred to as the $Pm-3m$ space group are considered and discussed in detail in the next section. The

extracted refined parameters are listed in Tables 2 and 3. The obtained lattice parameter is $a = b = c = 3.9796(1) \text{ \AA}$ and $3.9772(1) \text{ \AA}$ for $x = 0.2$ and 0.3 , respectively. Due to the smaller difference in ionic radii (16 pm) of Bi^{3+} (1.03 \AA) and Pb^{2+} (1.19 \AA), the lattice parameter did not show considerable variation with x in the PBFW material and is in well agreement with XRD results. The equivalent thermal vibrations of the ‘A’, ‘B’, and ‘O’ atoms are represented by the B_{iso} thermal parameter, which explains the motion of atoms from their equilibrium site, potential energy, and shape of the atomic site. The $B_{\text{iso}}(\text{\AA}^2)$ values of $\text{Pb}^{2+}/\text{Bi}^{2+}$, $\text{Fe}^{3+}/\text{W}^{6+}$, and O^{2-} atoms are listed in Tables 2 and 3. The Pb/Bi and O atoms exhibit the larger thermal parameter values indicating larger displacements from their equilibrium position (000) and $(\frac{1}{2} \frac{1}{2} 0)$, respectively. The Pb/Bi and O atoms thermally oriented along with the $[111]$ crystallographic directions and distorted in the (110) plane, respectively; hence, it leads to the ferroelectric behavior [56] (Fig. 2).

3.1.2 Scanning Electron Microscopy

Figure 3a and b depict the surface morphology of PBFW solid solutions studied through the SEM technique. The images show the uniform grains with the grain size of 1–2 μm , which represents the bulk nature of the synthesized materials. The synthesized samples show closely arranged grains with a small amount of porosity, which is well-matched with the density of materials as calculated in the XRD measurement. Investigation of the stoichiometric elemental compositions of the materials was done by the energy-dispersive X-ray analysis (EDAX) as shown in Fig. 3c and d. The obtained elemental ratio is observed to be nearly balanced with the stoichiometry of the precursors.

3.1.3 Raman Spectroscopy Studies

Room-temperature micro Raman studies were carried out for both $x = 0.2$ and $x = 0.3$ PBFW solid solutions using 785-nm

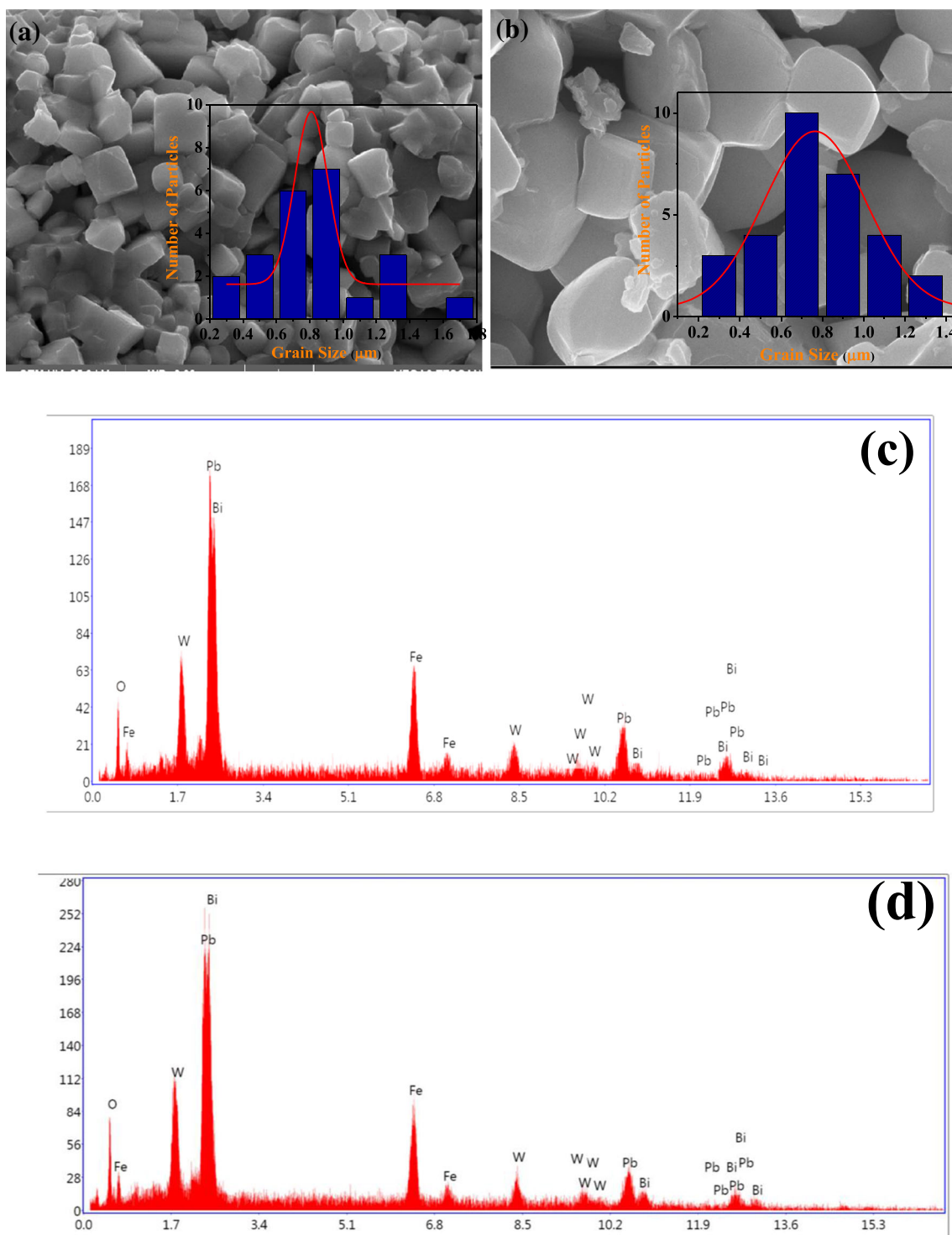


Fig. 3 SEM images (a, b) and EDAX patterns (c, d) of $(\text{PFW})_{1-x}(\text{BFO})_x$ for $(x = 0.2 \text{ and } 0.3)$

wavelength of He–Ne laser of power 100 mW and are shown in Fig. 4. It is known to be a very useful technique to investigate the local structural information of the complex disordered $A(\text{B}'\text{B}'')\text{O}_3$ perovskite structure. However, for the $Pm\text{-}3m$ space group first-order Raman modes are inactive, the PFW system exhibits the Raman peaks attributed to the local

structural distortion leads to nano polar-regions. Similar Raman peaks were observed in other Pb-based systems like $\text{Pb}(\text{Mg}_{1/3}\text{Nb}_{2/3})\text{O}_3$ [57–60], $\text{Pb}(\text{Sc}_{1/2}\text{Nb}_{1/2})\text{O}_3$ [60, 61], and $\text{Pb}(\text{Zn}_{1/3}\text{Nb}_{2/3})\text{O}_3$ [62]. One can observe a broad Raman band at a lower wavenumber regime of about 217.25 cm^{-1} related to the Pb–O asymmetric localized mode (F_{2g}) and peaks in the

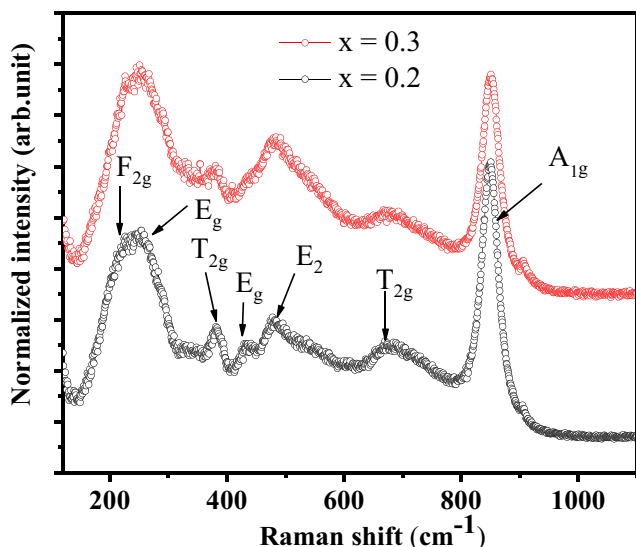


Fig. 4 RT Raman spectra of the (PFW)_{1-x}(BFO)_x for $x = 0.2$ and $x = 0.3$ solid solutions

300–500 cm^{-1} range assigned to the disorder-induced modes. The BO_6 octahedral distortion-related bending modes of W-O (T_{2g}) and Fe-O (E_g) were observed at 382.25 cm^{-1} and 428.54 cm^{-1} , respectively. The observation of well-pronounced peaks at 680.04 and 848.76 cm^{-1} is attributed to the $\text{B}'\text{-O-B}''$ octahedral modes, i.e., stretching vibration modes of W-O (T_{2g}) and $\text{Fe}^{3+}\text{-O-W}^{6+}$ (A_{1g}), respectively. The above-obtained modes indicate the formation of $\text{A}(\text{B}'\text{B}'')\text{O}_3$ perovskite structure [13] without any secondary phases.

It is worthy to note that the PFBW solid solutions exhibit the structural transition from pseudocubic to rhombohedral ($R3c$) as increasing the BFO composition by observing the anomalies as given below.

- 1) The Pb-O -related band at 217.25 cm^{-1} shows the sharpening and shifting from 217.25 to 227.33 cm^{-1} due to the increased concentration of Bi at A site.

- 2) A decrease in the intensity and broadening of the peaks at 382.25 cm^{-1} , 680.04, and 848.76 cm^{-1} due to lowering of the tungsten (W) concentration at the cation B'' site.
- 3) By making the solid solution, Fe occupies 2 positions, one in PFW octahedral and another one at BFO octahedral. Especially, the peak at 477.08 cm^{-1} (E_2) [63] is originated from the Fe-O rotationally distorted in the BiFeO_3 structure. In this, one can observe the decreasing intensity of 428.54 cm^{-1} attributed to the bending Fe-O (PFW) mode (E_g), and its intensity rises as Fe concentration raises in B' site.

3.1.4 Temperature-Dependent Neutron Diffraction Studies

The temperature evolution NPD of $(\text{PFW})_{1-x}(\text{BFO})_x$ solid solutions were measured in the temperature range 300–523 K and 300–623 K for $x = 0.2$ and 0.3 , respectively (Fig. 5a, b). The peaks at 2θ of 15.68°, 29.77°, 39.15°, and 47.94° correspond to the magnetic reflections (100), (200), (220), and (300), respectively. One can observe that the intensity of the magnetic reflections decreases with rising the temperature and vanishes above a temperature, indicates the onset of magnetic transition in both the samples. These samples have a commensurate G-type antiferromagnetic structure and will be discussed in detail in the following section.

Figure 6a and b represent the neutron powder diffraction patterns with profile fits between the observed and calculated profiles by the Rietveld refinement. Refinement of the NPD data for the nuclear structure was done by considering initial parameters like lattice parameters and atomic coordinates as obtained from the RT XRD refinement and the nuclear structure was refined by considering the Wyckoff positions as mentioned earlier. The magnetic structure, for magnetic reflections appearing at the different 2θ positions than the nuclear peaks, was refined by considering the $P-1$ magnetic symmetry space group and indexed with the propagation wave vector $k = (\frac{1}{2} \frac{1}{2}$

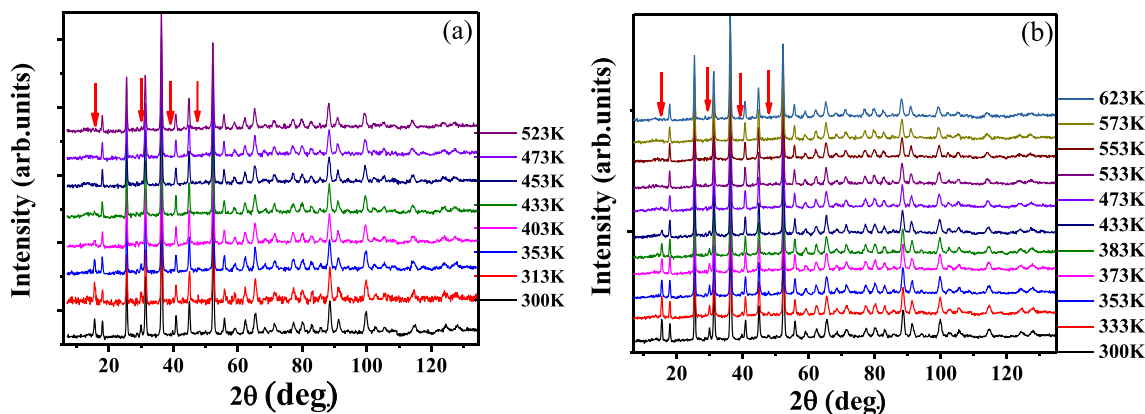


Fig. 5 Raw data of temperature-dependent NPD pattern for $(\text{PFW})_{1-x}(\text{BFO})_x$ a $x = 0.2$ at 300–523 K and b $x = 0.3$ at 300–623 K and downward arrow mark represents the magnetic Bragg reflections

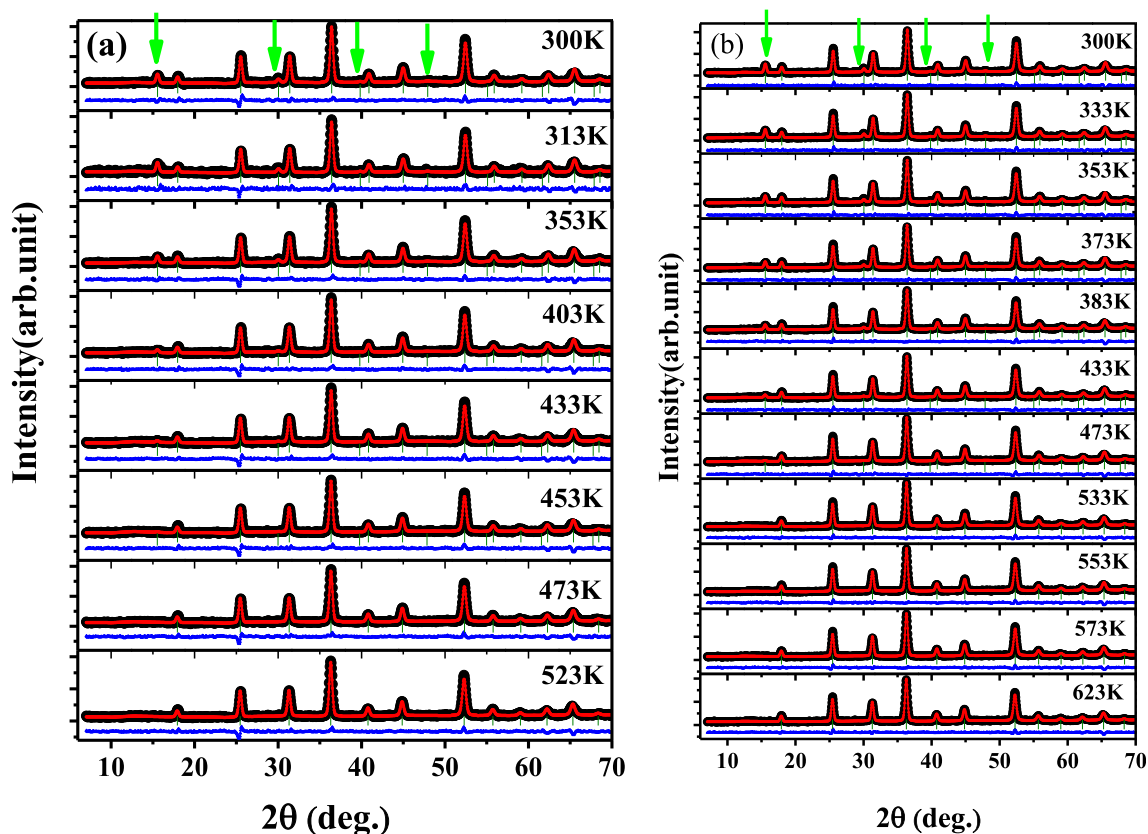


Fig. 6 Temperature variation of magnetic moment obtained in the NPD data for $(\text{PFW})_{1-x}(\text{BFO})_x$ **a** $x = 0.2$, **b** $x = 0.3$

$\frac{1}{2}$). This wave vector indicates the magnetic unit cell is double that of the $Pm\text{-}3m$ nuclear structure and with G-type antiferromagnetic ordering. The values of weighted χ^2 , R_{wp} , and R_{mag} factor parameters are well consistent with other reported results [54]. Refined parameters, lattice parameter, bond length (Pb/Bi–O and Fe/W–O), volume, and isothermal parameters (B_{iso}) are listed in Tables 2 and 3. The obtained B_{iso} values are larger for Pb/Bi and O atoms compared to B-site atoms (Fe/W); hence, we conclude that the structural distortions are due to the displacement of the Pb/Bi atoms in the [111] crystallographic directions from its equilibrium position and O atoms in the (110) plane [55]. This leads to the macroscopic ferroelectric spontaneous polarization in the samples.

The extracted temperature-dependent lattice parameters, bond length, and volume of the samples $x = 0.2$ and 0.3 are plotted in Fig. 7(a, b). It is evident from the figure that there is a presence of an increase in refined lattice parameters as increasing the temperature, linear lattice thermal expansion, along with the significant small discontinuous change (indicated by black arrows) at the magnetic transition $T_N = 435$ K and 504 K for $x = 0.2$ and 0.3 , respectively. This variation at the magnetic transition (T_N) reveals the existence of spin-lattice coupling due to the changing of spin configuration modify the lattice parameters in the ordered magnetic phase without affecting the structure. The thermal variation of Pb/Bi–O bond length largely affected the electric dipole moment, which leads to the magnetoelectric effect in the

multiferroics and hence shows the correlation between charge-lattice degrees of freedom.

The obtained magnetic structure suggests the presence of G-type antiferromagnetism and orienting of the magnetic moments along the c -axis or [001] direction of the pseudocubic crystal system as shown in Fig. 2b. However, the presence of antiferromagnetism having the residual magnetic moment due to the existence of Fe–O–Fe superexchange interaction between electrons in the $3d^5\text{-}2p^2$ orbitals, destruction of the spiral spin order in the BFO material and the existence of the cluster of magnetic nano regions in the disordered regime [54].

Figure 8a and b depict the temperature variation of the magnetic moment obtained from the NPD refinement for $x = 0.2$ and 0.3 samples. The magnitude of the obtained magnetic moment reduced as rising the temperature represents the lowering of exchange interaction energy ($\text{Fe}^{3+}\text{-O-Fe}^{3+}$) than the thermal energy. This manifests the onset of magnetic transition temperature $T_N = 435$ and 504 K for $x = 0.2$ and 0.3 , respectively. These disordered systems show a small residual moment above the T_N due to the sublattice uncompensated magnetic moment. By making the solid solutions, it is observed that the obtained magnetic moment at RT is $1.40(2)$ and $1.55(1) \mu_B/\text{Fe}$ for $x = 0.2$ and 0.3 , respectively. These magnetic moments are nearly 30% of the calculated values of $\mu_{\text{eff}} = 5\mu_B/\text{Fe}$ ($S = 5/2$, high spin state). These values are higher than the host PFW multiferroic material and also observed that the magnetic moment is increasing as x

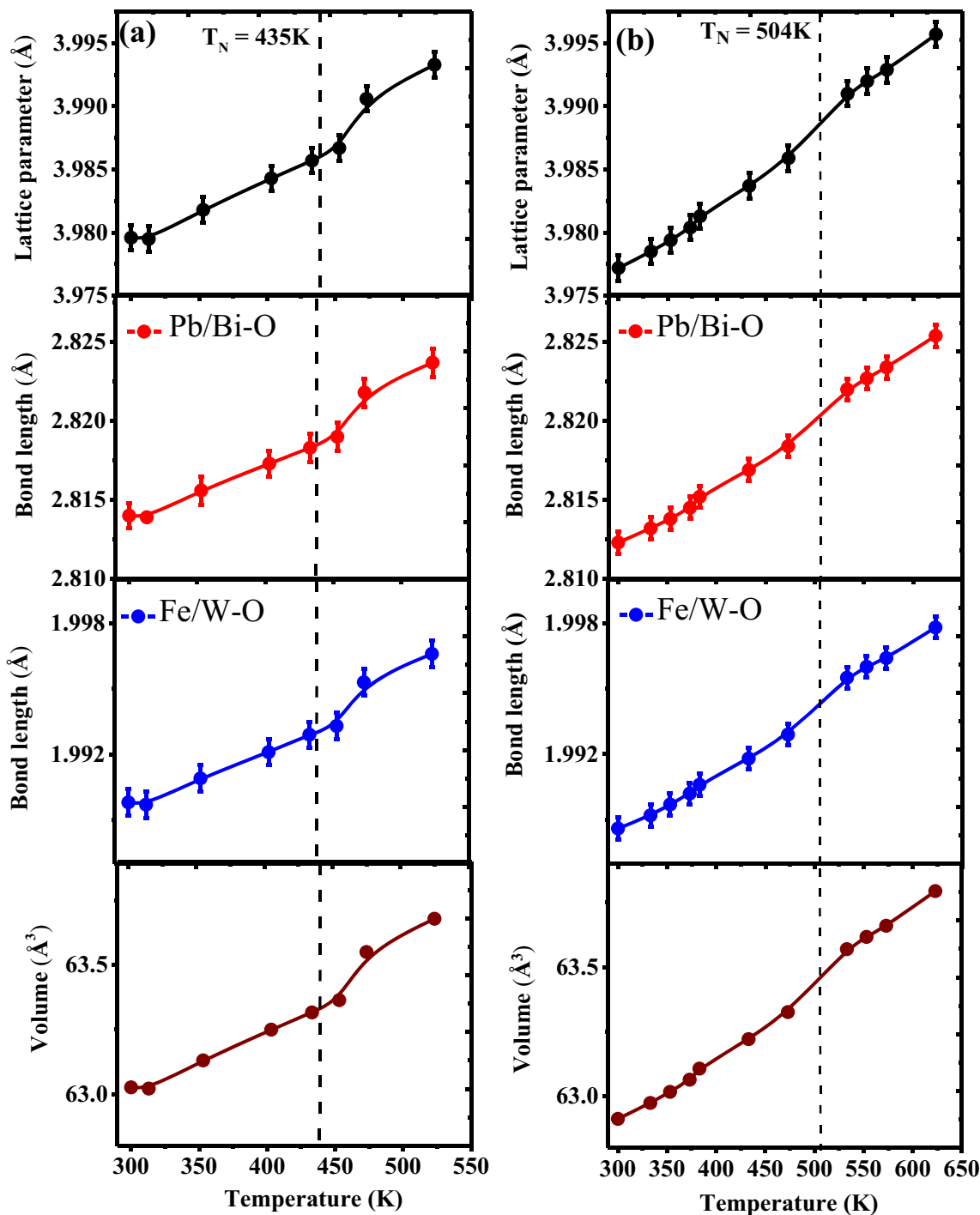


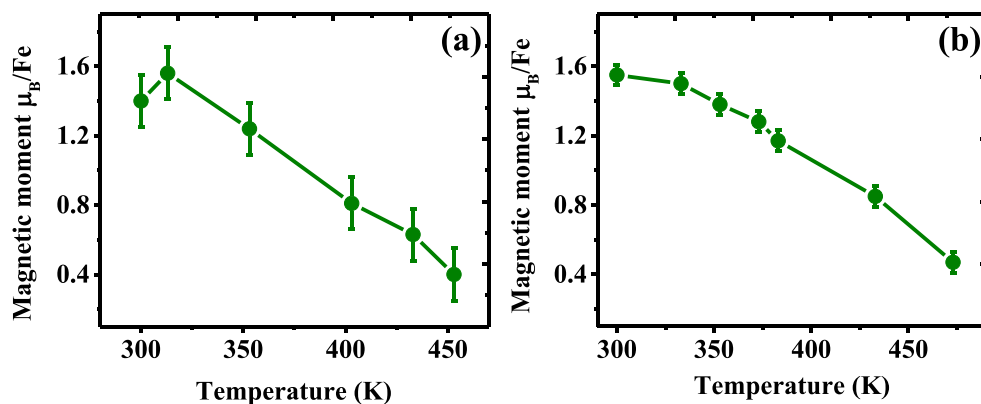
Fig. 7 Temperature dependence of ZFC and FC magnetic susceptibility curves at $H = 500$ Oe for $(\text{PFW})_{1-x}(\text{BFO})_x$ **a** $x = 0.2$ and **b** $x = 0.3$. Temperature vs inverse susceptibility ZFC curves for **c** $x = 0.2$ and **d**

$x = 0.3$ solid solution and red solid line correspond to the Curie-Weiss law fit and inset shows the derivative of magnetic susceptibility

growing [54]. One can observe the sudden decrease in the magnetic moment around 435 K and 504 K for $x = 0.2$ and 0.3, respectively, then it vanishes above this temperature which indicates the magnetic transition temperature (T_N) from antiferromagnetic to paramagnetic phase. Increasing the BFO composition enhances the magnetic transition T_N of the solid solutions

due to the increasing strength of the exchange interaction (J_{ex}) between the Fe–O–Fe path in the superexchange interaction, and it has a higher $T_N = 643$ K. Due to the rising of Fe concentration at the B-site of the perovskites, the distance between Fe–Fe ions and magnetic dilution reduces, hence raises the exchange interaction [64].

Fig. 8 M - H hysteresis curves at a selected temperature for $(\text{PFW})_{1-x}(\text{BFO})_x$ **a** $x = 0.2$ and **b** $x = 0.3$ solid solutions and insets show the magnified images of the M - H curves



The lattice parameter variation at the ferroelectric and magnetic transition shows the direct evidence of magnetoelectric coupling through the spin-lattice coupling in the system.

3.1.5 DC Magnetization Measurement

The DC magnetic susceptibility (χ vs T) was measured in the temperature range of 300–800 K at the 500 Oe field for PBFW solid solutions and presented in Fig. 9a and b. The observed χ (T) curves are not like that of typical antiferromagnetic

materials. The typical antiferromagnetic materials exhibit the magnetic transition peak at T_N ; in contrast, the PBFW ceramics show a continuous increase of magnetization below the transition temperature. Similar behavior was observed in some ferromagnetic, ferrimagnetic, or canted antiferromagnetic systems [65, 66]. In particular, $\text{Pb}(\text{Fe}_{2/3}\text{W}_{1/3})\text{O}_3$ belongs to the systems of disordered B-site cations with $\text{A}(\text{B}'\text{B}'')\text{O}_3$ perovskite structure and both B' and B'' cations are arranged in 1:1 (Fe^{3+} and W^{6+}) ordered manner in the B-site of few nanometer range [19, 20]. This kind of sub-nanoregions results in

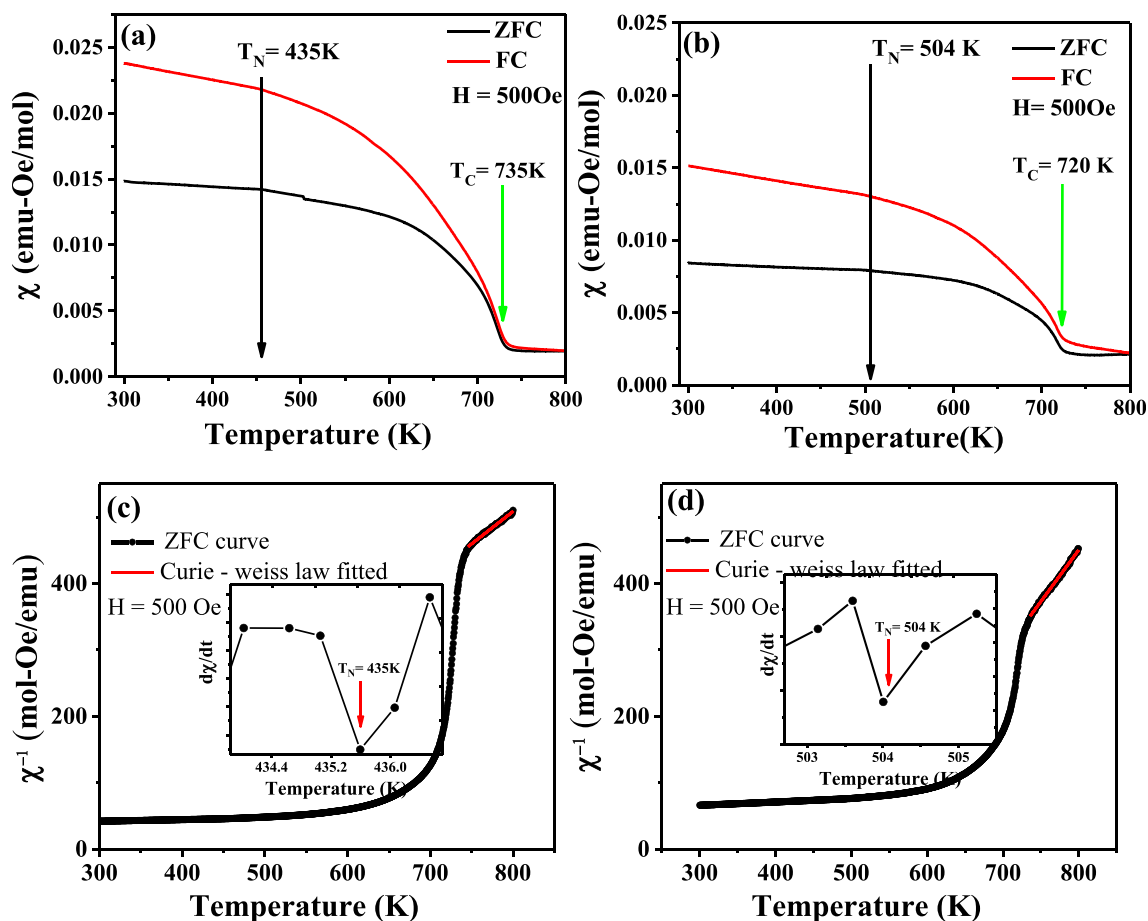


Fig. 9 Electron paramagnetic resonance spectra at different temperatures for $(\text{PFW})_{1-x}(\text{BFO})_x$ for a $x = 0.2$ and b $x = 0.3$

Table 4 Curie-Weiss law fitted parameters for (PFW)_{1-x}(BFO)_x solid solutions (x = 0.2 and 0.3)

Composition	T _C (K)	θ _p (K)	μ _{eff} (μ _B /Fe)	f = θ _p /T _C
x=0.2	735	-272.20	2.86	0.370
x=0.3	720	-510.15	2.26	0.708

the ferrimagnetic ordering in the antiferromagnetically interacting Fe³⁺ spins. Raevski et al. [67] explain theoretically the possible different chemical ordering of the nanoregions (Fig. 3 in ref. [67]), in which the PFB2 superstructure has close energy to the PFB5 ground state. Kuzian et al. [68] explain the magnetic properties of the PFB2 structure in which Fe ion has 2 inequivalent positions Fe1(up spin) at the center (Fig. 1b in ref. [68]) and Fe2 (down spin) shared in corner sites of the superstructure and other sites are filled with the non-magnetic W ion. These nano-size PFB2 ferrimagnetic ground-state structure interacting with superexchange interaction produce the uncompensated moment with the magnetic moment of 2.5μ_B/Fe ion; this is well matched with our magnetic moment obtained in the Neutron diffraction data. Hence, we conclude that the obtained temperature variation of magnetization is following the ferrimagnetic kind of behavior. Due the non-magnetic B" cation causes the magnetic dilution in the system arising from breaking the infinite long-range antiferromagnetic ordering and forms the nanoscale magnetic clusters which have more probability to exhibit the ferrimagnetic behavior. One can observe the larger magnetic transition temperature T_C (as shown by the green arrow marks in Fig. 9a, b) from ferrimagnetic to paramagnetic order around 735 and 720 K for x = 0.2 and 0.3, respectively. Due to the dominance of ferrimagnetic behavior, we observed small anomaly of

antiferromagnetic transition temperature T_N (as shown by the black arrow marks at 435 K and 504 K for x = 0.2 and 0.3, respectively (Fig. 9a, b)) and also depicted by plotting the derivative of magnetic susceptibility, as shown in the inset of Fig. 9c and d in the bulk magnetic measurement. Hence, we conclude that ferrimagnetic behavior persists above the T_N, as also observed in Fig. 8a and b. The field cooled curve shows the increasing trend of magnetization with decreasing temperature also reveals the canted antiferromagnetic behavior and destruction of spiral spin order in the BFO.

The measured ZFC and FC curves show the large difference in the magnetic moments which can be attributed to the magnetic irreversibility associated with the magneto-crystalline anisotropy of the materials [69]. The applied magnetic field is larger than the coercive field (H_C), shown in Table 5; hence, the magnetic moment rises as lowering the temperature below the magnetic transition temperature in the ZFC curve, thus χ_{FC} ∝ H_c⁻¹(T) [69].

The inverse magnetic susceptibility varies with temperature as shown in Fig. 9c and d. The paramagnetic region, around 740–800 K, is fitted with Curie-Weiss law, Eq. (1), and obtained the Curie-Weiss constant (C) and Curie-Weiss temperature (θ_p) and calculated the magnetic frustration (f = θ_p/T_C), listed in Table 4.

$$\chi = \frac{C}{T - \theta_p} \tag{1}$$

The negative value of θ_p indicates the antiferromagnetic nature of the materials, and the frustration “f” value less than 1 reveals the presence of frustration originating from the competitive interaction between the canted antiferromagnetism and ferrimagnetism in the PFBW multiferroic material.

Figure 10a and b depict the isothermal magnetization variation with the magnetic field of ± 90 kOe at 300, 450, and

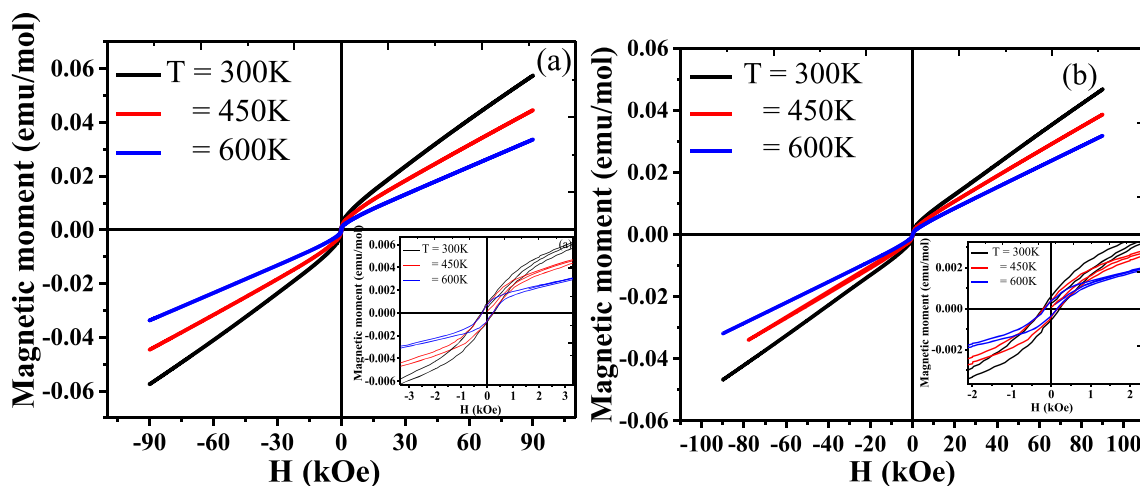


Fig. 10 Mössbauer spectra of (PFW)_{1-x}(BFO)_x for **a** x = 0.2 and **b** x = 0.3 at 300 K, **c** x = 0.2 and **d** x = 0.3 at 643 K; **e** temperature dependences of the Mössbauer spectrum intensity Im(T) related to their values at 673 K

Table 5 Remnant magnetization (M_r), saturation magnetization (M_s), and coercive field (H_c) of $(\text{PFW})_{1-x}(\text{BFO})_x$ solid solutions ($x = 0.2$ and 0.3) at different temperatures

Temperature (K)	Composition					
	$x=0.2$			$x=0.3$		
	M_r (emu/mol) $\times 10^{-4}$	M_s (emu/mol)	H_c (kOe)	M_r (emu/mol) $\times 10^{-4}$	M_s (emu/mol)	H_c (kOe)
300	8.8564	0.0036	0.1869	6.0615	0.0025	0.2097
450	7.2282	0.0033	0.1834	3.9100	0.0014	0.1994
600	6.6545	0.0020	0.2036	3.9851	0.0009	0.1879

600 K. The M vs H hysteresis curve shows the opening of loops only at the lower applied field, as shown in the inset of Fig. 10a and b, and non-linearity in the magnetic moment is associated with ferrimagnetic spin order evolved from the chemical ordering [70]. Hence, this ferrimagnetic contribution depends on the temperature; at lower fields, it is due to the complete alignment of ferrimagnetic spins and their forbidden motion. In the higher applied magnetic fields, the hysteresis loops show the linear and no saturation kind of behavior which is attributed to the $\text{Fe}^{3+}\text{--O--Fe}^{3+}$ antiferromagnetic interaction of the samples. The measured values of coercive field (H_c), saturation magnetization (M_s), and remnant magnetization (M_r) are listed in Table 5. The coercive field remains constant at all temperatures is responsible for the ferrimagnetic behavior at the lower field, whereas M_s and M_r slightly reduce as increasing the temperature and linear portion at higher field shows the presence of antiferromagnetism in both $x = 0.2$ and 0.3 .

3.1.6 Electron Paramagnetic Resonance

The electron paramagnetic resonance (EPR) measurement helps the microscopic understanding of static and dynamical spin-spin interactions of the magnetic materials, which is very sensitive to the electronic properties. Figure 11a and b depict

the variation of temperature-dependent EPR spectra of $x = 0.2$ and 0.3 in the X-band frequency range (8.75–9.65 GHz) at 300, 350, and 450 K. The observed dP/dH vs H signal seems to be Lorentzian-like behavior and also $x = 0.2$ exhibits the two absorption signals, one broader signal at the lower field (LF) of 50–100 mT range and Fe^{3+} ion-related narrower signal at the higher field (HF) at 330–370 mT range. The LF signal is attributed to the isolated Fe^{3+} ion located in the 1:1 B site cation magnetic environment with low symmetry, responsible for the ferrimagnetism and is in consistent with the magnetization results [70, 71]. The obtained slightly narrower HF resonance indicates the antiferromagnetic nature originated from the canting of spins in the $\text{Fe}^{3+}\text{--O--Fe}^{3+}$ interactions along with the paramagnetic clusters. Particularly, the $x = 0.3$ sample shows the splitting peaks in the HF, related to the Fe ion in the rhombohedral structure due to the higher BiFeO_3 concentration [72]. Table 6 shows the observed values of g , linewidth (ΔB_{p-p}), peak asymmetry (P_{assy}), and spin canting (D). The g -factor values deviated from free-electron $g_e \approx 2.003$ value which indicates the superexchange interaction results in the antiferromagnetic and anisotropic nature in the materials. For $x = 0.2$, g is less than g_e , and for $x = 0.3$, g is greater than g_e . With the increase in temperature, the value of g goes near to the value of g_e , represents the disorderness leads to the paramagnetic phase. This lower shift of g in the $x = 0.2$

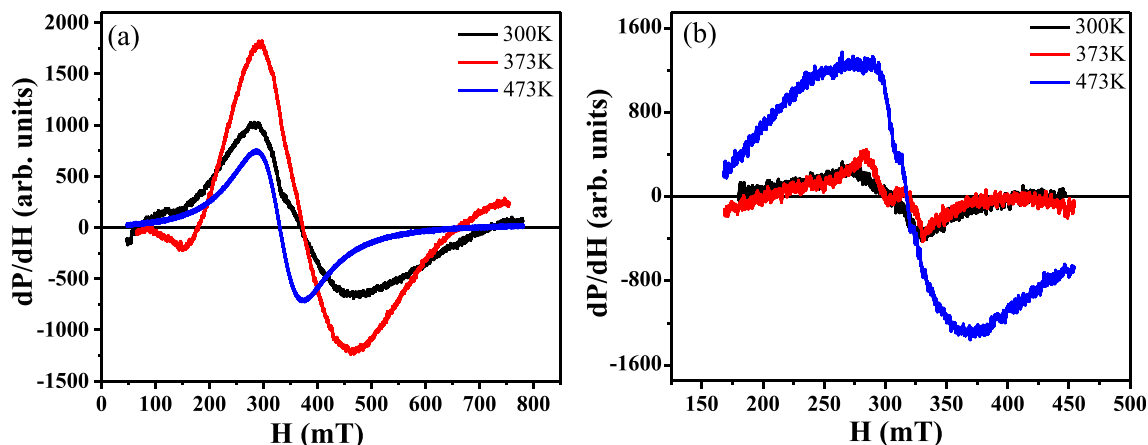


Fig. 11 Rietveld refined NPD data at different temperature for $(\text{PFW})_{1-x}(\text{BFO})_x$ a $x = 0.2$ and b $x = 0.3$ solid solution

Table 6 Lande g factor (g), Lande g factor ratio ($\Delta g/g$), peak width, and P_{asy} parameters obtained from the observed EPR spectra of $(PFW)_{1-x}(BFO)_x$ solid solutions at different temperature

Composition	300 K				373 K				473 K			
	g	$\Delta g/g$	ΔB_{p-p} (mT)	P_{asy}	g	$\Delta g/g$	ΔB_{p-p} (mT)	P_{asy}	g	$\Delta g/g$	ΔB_{p-p} (mT)	P_{asy}
$x=0.2$	1.765	0.134	187.878	0.469	1.745	0.147	170.393	0.496	1.969	0.017	89.299	0.051
$x=0.3$	2.129	0.059	61.885	0.237	2.112	0.051	47.864	0.127	2.046	0.021	80.517	0.023

is due to the ferroelectric transition at 285 K, and space charge relaxation in the 350–450 K range affects the g value [73]. Moreover, the peak-to-peak linewidth (ΔB_{p-p}) of each sample shows the temperature variation, which correlated with the spin-spin and spin-lattice interactions. In $x = 0.2$, as the temperature decreases, the signal becomes broader, which represents the presence of magnetic moment originated from the canted antiferromagnetic spins. The EPR linewidth is associated with the conductivity of the charge carriers; hence, $x = 0.3$ shows the larger linewidth at 473 K instead of a lower value. Usually, as the temperature increases, the signal becomes narrower due to the increase of disorderliness from the thermal agitation, but the system exhibits the hopping conduction mechanism of the space charges in that temperature range; therefore, we observed the larger value of ΔB_{p-p} [74]. This increasing trend leads to the larger spin-lattice interaction in the PFW samples. When the signals of $x = 0.2$ and 0.3 samples are compared, we observed that $x = 0.2$ system shows a higher value due to the presence of ferroelectricity and space charge relations. The symmetry behavior can be calculated from $P_{asy} = (1 - \frac{h_u}{h_l})$; h_u and h_l height of the upper and lower

peak, respectively. One can observe the asymmetric nature of the EPR signals in both the compositions at all the temperature, which reveals the presence of the magneto-crystalline anisotropic character of the samples. Usually, asymmetric behavior is observed in bulk samples. It decreases as raising the temperature due to the paramagnetic behavior and also decreases with the composition due to the conduction electron interaction with phonons at the T_C and the presence of space charge polarization in that temperature region [75].

3.1.7 Mössbauer Spectroscopy

Room temperature Mössbauer spectra of $(1-x)Pb(Fe_{2/3}W_{1/3})O_{3-x}BiFeO_3$ ($x = 0.2$ and 0.3) solid solution samples are Zeeman sextets (Fig. 12a, b). The parameters of spectra are listed in Table 7. The isomer shift value of sextet corresponds to the Fe^{3+} in oxygen octahedron [76]. The hyperfine magnetic field values of the spectra are increasing with x growing. This increase is determined by the growth of Fe^{3+} concentration and reduced lattice parameters in the samples. At 673 K, the Mössbauer spectra of PFW solid solution

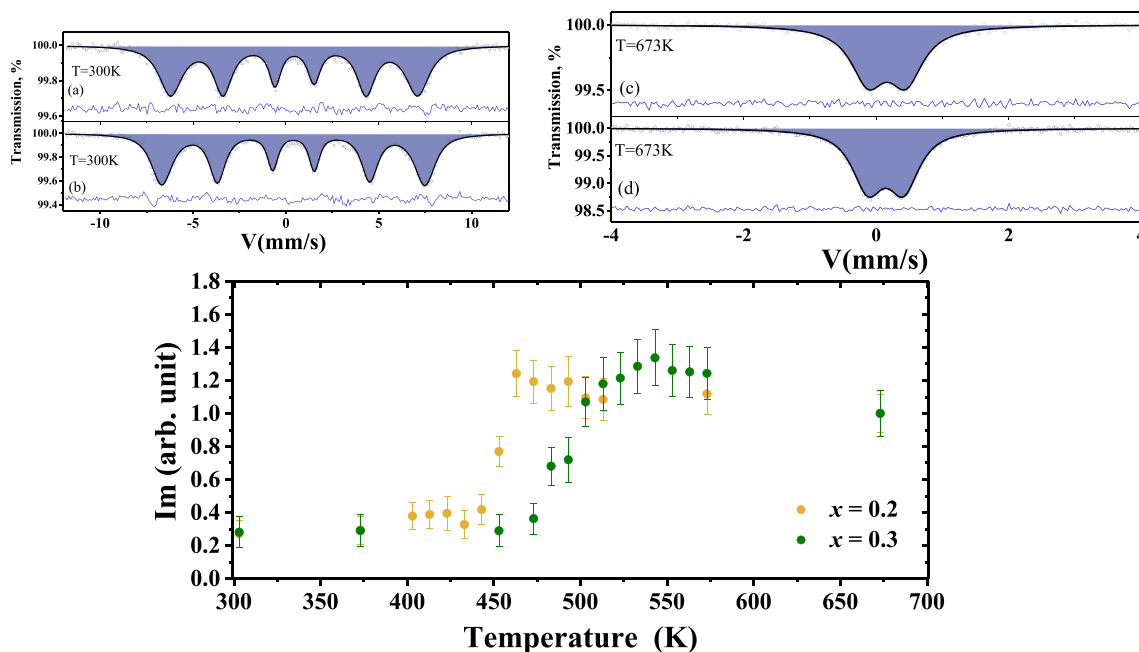


Fig. 12 Temperature-dependent structural parameters for (a) $x = 0.2$ and (b) $x = 0.3$ solid solutions

Table 7 Parameters of $(\text{PFW})_{1-x}(\text{BFO})_x$ Mössbauer spectra taken at room temperature and 673 K

x	T (K)	Component	$\delta \pm 0.02$ (mm/s)	$\epsilon/\Delta \pm 0.02$, (mm/s)	$H \pm 0.1$, T	$G \pm 0.02$, (mm/s)
0.2	300	Sextet	0.45	−0.01	41.2	1.49
	673	Doublet	0.16	0.57		0.62
0.3	300	Sextet	0.41	−0.01	43.9	1.35
	673	Doublet	0.15	0.54		0.57

δ , isomer shift; ϵ , quadrupole shift; Δ , quadrupole splitting for paramagnetic component; H , hyperfine magnetic field on ^{57}Fe nucleus; G , linewidth

samples are represented by the paramagnetic doublet (Fig. 12c, d). The quadrupole splitting values (Δ) of the doublets depend on the symmetry of Fe^{3+} nearest environment. The lower the local symmetry of Fe^{3+} ions, the greater the Δ is. The Δ values of PBFW samples decrease with x growing. This indicates the growth of the local environment symmetry of Fe^{3+} ions. Moreover, the linewidth of the doublet lines becomes narrower with x growing. The line broadening of doublet lines associates with the crystal inhomogeneity of the samples. Therefore, the cation substitutions in PBFW solid solution lead to the growth of local symmetry and homogeneity of the Fe^{3+} nearest environment.

The transformation of the Mössbauer spectrum from doublet to sextet near the magnetic phase transition temperature allows one to estimate the Neel temperature (T_N) of the PBFW solid solution samples. This transformation is accompanied by the decrease in the magnitude Im of the Mössbauer spectrum line intensity. To get the magnitude of Mössbauer line intensity, the number of pulses in the velocity range of -0.5 – 0.5 mm/s and 12 mm/s was measured. The difference between pulse number is equal to the Im . Measuring Im in the course of sequential decrease in temperature allows one to get its temperature dependence. The drop on the $Im(T)$ corresponds to the T_N value. This approach has been successfully used to determine the T_N in the perovskite compounds [77–79].

Figure 12e shows the temperature dependence of Im (T) related to its value at 463 K for the $(\text{PFW})_{1-x}(\text{BFO})_x$ ($x = 0.2$ and 0.3) solid solution samples. The middle of the drops on the $Im(T)$ corresponds to the T_N values. As can be seen from Fig. 12e, the $T_N \approx 435$ K for $x = 0.2$ and $T_N \approx 504$ K for $x = 0.3$. The magnetic order of the perovskite-like compounds is determined by the number of $\text{Fe}^{3+}\text{--O--Fe}^{3+}$ links and the distance between Fe^{3+} ions [80]. Thus, the increase in T_N values is caused by the growing concentration of Fe^{3+} ions.

4 Conclusions

RT single-phase multiferroic materials, $(\text{PFW})_{1-x}(\text{BFO})_x$ ($x = 0.2$ and $x = 0.3$) solid solutions, were synthesized by the columbite solid-state reaction method. The Rietveld refinement of RT XRD

and NPD of the samples shows the pseudocubic crystal symmetry without any secondary phases. The SEM study confirms the bulk nature of the ceramic materials. The micro Raman studies reveal the structural changes from pseudocubic to rhombohedral, as seen from the A (Pb/Bi–O) and B (Fe/W–O) site atoms related modes. A small discontinuous change at the antiferromagnetic onset temperature (T_N) in the lattice parameters, extracted from the temperature evolution of NPD data, reveals the presence of magnetoelectric coupling through the spin-lattice coupling. Temperature variation of magnetic moment exhibits a sudden decrease at the onset of magnetic transition temperature $T_N = 435$ K and 504 K for $x = 0.2$ and 0.3 , respectively. The PBFW solid solutions astonishingly exhibit the ferrimagnetic kind of behavior in the bulk magnetization measurement curves and which was also evident from the opening of M vs H loops at the lower field regime. This arises from 1:1 B-site-ordered local arrangement in these relaxor type materials. The linear behavior in the M–H loops as increasing the field reveals the presence of antiferromagnetism. The Mössbauer spectroscopy shows the Fe in +3 state and G-type antiferromagnetic structure. However, the broad signal in EPR and sextet nature in Mössbauer spectra reveals the presence of residual magnetic moment in the materials. These signatures also indicate the presence of the B-site disorderliness, which induces the ferrimagnetism and can be observed as a small resonance signal at the higher field in the EPR ($x = 0.2$) spectra.

Acknowledgments The authors (SI, SM, and BA) thank UGC-DAE-CSR, Mumbai Centre, for the financial support and experimental facilities through the CRS-M-200 project. The author (SI) thanks the Council of Scientific and Industrial Research (CSIR), New Delhi, for the SRF award. The author (SM) thanks the Vision Group on Science and Technology (VGST) Government of Karnataka for sanctioning the project in “Center for Excellence in Science Engineering and Medicine.” Also, the authors thank the DST-FIST and UGC-CPEPA program for providing XRD and Raman facilities, respectively, at the Department of Physics, Bangalore University, Bengaluru. Dr. SP Kubrin acknowledges the financial support from the Ministry of Science and Higher Education of the Russian Federation (State assignment in the field of scientific activity, Southern Federal University, 2020).

Compliance with Ethical Standards

Conflict of Interest The authors declare that they have no conflict of interest.

References

- Schmid, H.: Multiferroic magnetoelectrics. *Ferroelectrics*. **162**, 317–338 (1994)
- Fiebig, M.: Revival of the magnetoelectric effect. *J. Phys. D*. **38**, R123–R152 (2005)
- Fiebig, M., Lottermoser, T., Meier, D., Trassin, M.: The evolution of multiferroics. *Nat. Rev. Mater.* **1**, 1–14 (2016)
- Spaldin, N.A.: Multiferroics: past, present, and future. *MRS Bull.* **42**, 385–390 (2017)
- Spaldin, N.A., Ramesh, R.: Advances in magnetoelectric multiferroics. *Nat. Mater.* **18**, 203–212 (2019)
- Tokura, Y., Seki, S., Nagaosa, N.: Multiferroics of spin origin. *Rep. Prog. Phys.* **77**, 76501–76545 (2014)
- Ramesh, R., Spaldin, N.A.: Multiferroics: progress and prospects in thin films. *Nat. Mater.* **6**, 21–29 (2007)
- Nicola, A.: Hill, why are there so few magnetic ferroelectrics? *J. Phys. Chem. B*. **104**, 6694–6709 (2000)
- S.M. Skinner, Magnetically ordered ferroelectric materials, *IEEE Trans. Parts Mater. Packag.* **6** [2], 68–90 (1970)
- G.A. Smolenskii, I.E. Chupis, *Sov. Phys. Ferroelectromagnets, Uspekhi* **25**, 475 (1982)
- Ye, Z.-G., Schmid, H.: *Ferroelectrics*. **162**, 119 (1994)
- Nathascia Lampis, Philippe Sciau and Alessandra Geddo Lehmann, Rietveld refinements of the paraelectric and ferroelectric structures of $\text{PbFe}_{0.5}\text{Ta}_{0.5}\text{O}_3$, *J. Phys.: Condens. Matter* **12**, 2367–2378 (2000)
- Matteppanavar, S., Rayaprol, S., Angadi, B., Sahoo, B.: Composition dependent room temperature structure, electric and magnetic properties in magnetoelectric $\text{Pb}(\text{Fe}_{1/2}\text{Nb}_{1/2})\text{O}_3$ - $\text{Pb}(\text{Fe}_{2/3}\text{W}_{1/3})\text{O}_3$ solid-solutions. *J. All. Comp.* **677**, 27–37 (2016)
- Brixel, W., Rivera, J.P., Steiner, A., Schmid, H.: Magnetic field induced magnetoelectric effects, $(\text{ME})_{\text{H}}$, in the perovskites Pb_2CoWO_6 and $\text{Pb}_2\text{FeTaO}_6$. *Ferroelectrics*. **79**, 201–204 (1988)
- Setter, N., Cross, L.E.: The role of B-site cation disorder in diffuse phase transition behavior of perovskite ferroelectrics. *J. Appl. Phys.* **51**, 4356–4360 (1980)
- Mitoseriu, L., Marre, D., Siri, A.S., Nanni, P.: Magnetic properties of $\text{PbFe}_{2/3}\text{W}_{1/3}\text{O}_3$ - PbTiO_3 solid solutions. *J. Appl. Phys.* **83**, 5509–5511 (2003)
- Smolenski, G.A., Agranovskaya, A.I., Isupov, V.A.: *Sov. Phys. Sol. State*. **1**, 907 (1959)
- Smolenskii, G.A.: *J. Phys. Soc. Jpn. (Suppl.)*. **28**, 26 (1970)
- Baettig, P., Spaldin, N.A.: Ab initio prediction of a multiferroic with large polarization and magnetization. *Appl. Phys. Lett.* **86**, 012505–012503 (2005)
- W. Qu, X. Tan, R. W. McCallum, D. P. Cann and E. Ustundag, Room temperature magnetoelectric multiferroism through cation ordering in complex perovskite solid solutions. *J. Phys.: Condens. Matter* **18**, 8935–8942 (2006)
- Ivanov, S.A., Eriksson, S.G., Tellgren, R., Rundlof, H.: Nuclear and magnetic structure of $\text{Ba}_3\text{Fe}_2\text{WO}_9$. *Mater. Res. Bull.* **39**, 615–628 (2004)
- Farber, L., Valant, M., Akbas, M.A., Davies, P.K.: Cation ordering in $\text{Pb}(\text{Mg}_{1/3}\text{Nb}_{2/3})\text{O}_3$ - $\text{Pb}(\text{Sc}_{1/2}\text{Nb}_{1/2})\text{O}_3$ (PMN-PSN) solid solutions. *J. Am. Ceram. Soc.* **85**, 2319–2324 (2002)
- Ivanov, S.A., Beran, P., Bush, A.A., Sarkar, T., Shafeie, S., Wang, D., Eriksson, O., Sahlberg, M., Kvashnin, Y., Tellgren, R., Nordblad, P., Mathieu, R.: Cation ordering, ferrimagnetism and ferroelectric relaxor behavior in $\text{Pb}(\text{Fe}_{1-x}\text{Sc}_x)_{2/3}\text{W}_{1/3}\text{O}_3$ solid solutions. *Eur. Phys. J. B*. **92**, 163–116 (2019)
- Tan, X., Wongmaneeerung, R., McCallum, R.W.: Ferroelectric and magnetic properties of $\text{Pb}(\text{Fe}_{2/3}\text{W}_{1/3})\text{O}_3$ -based multiferroic compounds with cation order. *J. Appl. Phys.* **102**, 104114–104116 (2007)
- Wongmaneeerung, R., Tan, X., McCallum, R.W., Ananta, S., Yimmirun, R.: Cation, dipole, and spin order in $\text{Pb}(\text{Fe}_{2/3}\text{W}_{1/3})\text{O}_3$ -based magnetoelectric multiferroic compounds. *J. Appl. Phys.* **90**, 242905–242903 (2007)
- Nechache, R., Hamagea, C., Pignolet, A., Normandin, F., Veres, T., Carignan, L.P., Menard, D.: Growth, structure, and properties of epitaxial thin films of first-principles predicted multiferroic $\text{Bi}_2\text{FeCrO}_6$. *Appl. Phys. Lett.* **89**, 102902–102903 (2006)
- Joshi, D.C., Ivanov, S.A., Bush, A.A., Sarkar, T., Ye, Z.-G., Nordblad, P., Mathieu, R.: Room temperature ferrimagnetism in Yb-doped relaxor ferroelectric $\text{PbFe}_{2/3}\text{W}_{1/3}\text{O}_3$. *Appl. Phys. Lett.* **115**, 072902–072904 (2019)
- Y.N. Venevtsev, E.D. Politova, S.A. Ivanov, Ferro- and Antiferroelectrics of Barium Titanate Family, *Chemistry*, 256 (1985)
- Yu. N. Venevtsev, V.V. Gagulin, V.N. Ljubimov, *Ferroelectromagnets*, 172(1982)
- Zhou, L., Vilarinho, P.M., Mantas, P.Q., Baptista, J.L., Fortunato, E.: The effects of La on the dielectric properties of lead iron tungstate $\text{Pb}(\text{Fe}_{2/3}\text{W}_{1/3})\text{O}_3$ relaxor ceramics. *J. Eur. Ceram. Soc.* **20**, 1035–1041 (2000)
- S.A. Ivanov, Magnetoelectric complex metal oxides: main features of preparation, structure and properties, in *Advanced Functional Materials*, edited by B. Sanyal, O. Eriksson, 163, 234–241 (2012) (Elsevier, Oxford, UK)
- R.N.P. Choudhary, D.K. Pradhan, C.M. Tirado, G.E. Bonilla, R.S. Katiyar, Impedance characteristics of $\text{Pb}(\text{Fe}_{2/3}\text{W}_{1/3})\text{O}_3$ - BiFeO_3 composites. *phys. stat. sol. (b)* **244**, 2254–2266 (2007)
- Fraygola, B., Eiras, J.A.: Effect of magnetic ion doping on structural, electric and relaxor properties of $\text{Pb}(\text{Fe}_{2/3}\text{W}_{1/3})\text{O}_3$ multiferroic ceramics. *Mater. Res.* **17**, 1594–1600 (2014)
- D. Lee, S.M. Yang, Y. Jo, T.K. Song, Room-temperature multiferroic properties of $\text{Pb}(\text{Zr}_{0.57}\text{Ti}_{0.43})\text{O}_3$ - $\text{Pb}(\text{Fe}_{0.67}\text{W}_{0.33})\text{O}_3$ solid-solution epitaxial thin films, *J. Korean Phys. Soc.* **57**, 1914–1918 (2010)
- Yokosuka, M., Kojima, H.: Dielectric and piezoelectric properties of the solid solution system $\text{Pb}(\text{Fe}_{2/3}\text{W}_{1/3})\text{O}_3$ - PbZrO_3 . *Jpn. J. Appl. Phys.* **36**, 6046–6050 (1997)
- S.A. Ivanov, P. Nordblad, R. Tellgren, T. Ericsson, H. Rundlof, Structural, magnetic and Mössbauer spectroscopic investigations of the magnetoelectric relaxor $\text{Pb}(\text{Fe}_{0.6}\text{W}_{0.2}\text{Nb}_{0.2})\text{O}_3$, *Solid State Sci.* **9**, 440–450 (2007)
- Szwagierczak, D., Kulawik, J.: Influence of MnO_2 and Co_3O_4 dopants on dielectric properties of $\text{Pb}(\text{Fe}_{2/3}\text{W}_{1/3})\text{O}_3$ ceramics. *J. Eur. Ceram. Soc.* **25**, 1657–1662 (2005)
- Zhou, L., Vilarinho, P.M., Baptista, J.L.: The characteristics of the diffuse phase transition in Mn doped $\text{Pb}(\text{Fe}_{2/3}\text{W}_{1/3})\text{O}_3$ relaxor ceramics. *J. Appl. Phys.* **85**, 2312–2317 (1999)
- Brzezinska, D., Skulski, R., Bochenek, D., Niemiec, P., Chrobak, A., Fajfrowski, L., Matyjasik, S.: The magnetic and electric properties of PZT-PFW-PFN ceramics. *J. Alloys Compd.* **737**, 299–307 (2018)
- Matteppanavar, S., Rayaprol, S., Angadi, B., Sahoo, B.: Evidence for room-temperature weak ferromagnetic and ferroelectric ordering in magnetoelectric $\text{Pb}(\text{Fe}_{0.634}\text{W}_{0.266}\text{Nb}_{0.1})\text{O}_3$, ceramic. *J. Supercond. Nov. Magn.* **30**(1317–1325), 1317 (2017)
- Vilarinho, P.M., Zhou, L., Pockl, M., Marques, N., Baptista, J.L.: Dielectric properties of $\text{Pb}(\text{Fe}_{2/3}\text{W}_{1/3})\text{O}_3$ - PbTiO_3 solid-solution ceramics. *J. Am. Ceram. Soc.* **83**, 1149–1152 (2000)
- Feng, L., Guo, H., Ye, Z.G.: Magnetic ordering in relaxor ferroelectric $(1-x)\text{Pb}(\text{Fe}_{2/3}\text{W}_{1/3})\text{O}_3$ - $x\text{PbTiO}_3$ single crystals. *J. Mater. Res.* **22**, 2116–2124 (2006)
- Dulkin, E., Mojaev, E., Roth, M., Kamba, S., Vilarinho, P.M.: Burns, Néel, and structural phase transitions in multiferroic $\text{Pb}(\text{Fe}_{2/3}\text{W}_{1/3})\text{O}_3$ - $x\text{PbTiO}_3$ detected by an acoustic emission. *J. Appl. Phys.* **103**, 083542–083545 (2008)

44. Lebeugle, D., Colson, D., Forget, A., Viret, M.: Very large spontaneous electric polarization in BiFeO₃ single crystal at room temperature and its evolution under cycling fields. *Appl. Phys. Lett.* **91**, 022907(1)–022907(3) (2007)
45. Kaczmarek, W., Pajak, Z., Polomska, M.: Differential thermal analysis of phase transitions in (Bi_{1-x}La_x)FeO₃ solid solutions. *Solid State Commun.* **17**, 807–810 (1975)
46. Azuma, M., Takata, K., Saito, T., Ishiwata, S., Shimakawa, Y., Takano, M.: Designed ferromagnetic ferroelectric Bi(2)NiMnO(6). *J. Am. Chem. Soc.* **127**, 8889–8892 (2005)
47. V. R. Palkar, D. C. Kundaliya, S. K. Malik, and S. Bhattacharya, Magnetolectricity at room temperature in the Bi_{0.9-x}Tb_xLa_{0.1}FeO₃ system, *Phys. Rev. B* **69**, 212102–3 (2004)
48. Singh, A., Senyshyn, A., Fuess, H., Chatterji, T., Pandey, D.: Neutron powder diffraction study of nuclear and magnetic structures of multiferroic (Bi_{0.8}Ba_{0.2})(Fe_{0.8}Ti_{0.2})O₃: evidence for isostructural phase transition and magnetoelastic and magnetoelectric couplings. *Phys. Rev. B.* **83**(054406–9), (2011)
49. I. Shivaraja, S. Matteppanvar, S. T. Dadami, S. Rayaprol, B. Angadi, Synthesis, structural and electron paramagnetic resonance studies on Pb_{0.9}Bi_{0.1}Fe_{0.7}W_{0.3}O₃ ceramic, *AIP. Con. Proceed.* **142**, 140015–4 (2018)
50. P.S.R. Krishna, A.B. Shinde, A. das, S.S. Naik, S.K. Pranjep and M. Ramanandham, *Sol.Sta.phy.* **45**,149, (2002)
51. J. Rodriguez-Carvajal Laboratory, FULLPROF, a Rietveld and pattern matching and analysis programs version 2018, Laboratoire Leon Brillouin, CEA-CNRS, France
52. Matsnev, M.E., Rusakov, V.S.: SpectRelax: an application for Mössbauer spectra modeling and fitting. *AIP. Con. Proceed.* **1489**, 178–174 (2012)
53. Rodriguez-Carvajal, J.: Recent advances in magnetic structure determination by neutron powder diffraction. *Physica B.* **192**, 55–69 (1993)
54. Shidaling Matteppanavar, Sudhindra Rayaprol, A.V. Anupama, Basavaraj Angadi, Balaram Sahoo, Origin of room temperature weak-ferromagnetism in antiferromagnetic Pb(Fe_{2/3}W_{1/3})O₃, *Cer. Inter.* **41**, 1–7 (2015)
55. R. N. P. Choudhary, Dillip K. Pradhan, C. M. Tirado, G. E. Bonilla, and R. S. Katiyara, Relaxor characteristics of Pb(Fe_{2/3}W_{1/3})O₃–BiFeO₃ solid solution prepared by mechanosynthesis route, *J. Appl. Phys.* **100**, 084105–8 (2006)
56. S.A. Ivanov, P. Nordblad, R. Tellgren, T. Ericsson, H. Rundlof, Structural, magnetic and Mössbauer spectroscopic investigations of the magnetoelectric relaxor Pb(Fe_{0.6}W_{0.2}Nb_{0.2})O₃, *Sol. Sta. Sci.* **9**, 440–450 (2007)
57. Husson, E., Abello, L., Morell, A.: Short-range order in PbMg_{1/3}Nb_{2/3}O₃ ceramics by Raman spectroscopy. *Mater. Res. Bull.* **25**, 539–545 (1990)
58. O. Svitelskiy, J. Toulouse, G Yong and Z. G. Ye, Polarized Raman study of the phonon dynamics in Pb(Mg_{1/3}Nb_{2/3})O₃ crystal, *Phys. Rev. B* **68**, 104107–10(2003)
59. Prosandeev, S.A., Cockayne, E., Burton, B.P., Kamba, S., Petzelt, J., Yuzuyuk, Y., Katiyar, R.S., Vakhrushev, S.B.: Lattice dynamics in Pb(Mg_{1/3}Nb_{2/3})O₃. *Phys. Rev. B.* **70**, 134110–134111 (2004)
60. Haumont, R., Gemeiner, P., Dkhil, B., Kiat, J.M., Bulou, A.: Polar and chemical states at a nanometer scale in a PbSc_{1/2}Nb_{1/2}O₃–PbTiO₃ system investigated by Raman spectroscopy. *Phys. Rev. B.* **73**, 104106–104105 (2006)
61. Zhu, M., Chen, C., Tang, J., Hou, Y., Wang, H., Yan, H., Zhang, W., Chen, J., Zhang, W.J.: Effects of ordering degree on the dielectric and ferroelectric behaviors of relaxor ferroelectric Pb(Sc_{1/2}Nb_{1/2})O₃ ceramics. *Appl. Phys.* **103**, 084124–084126 (2008)
62. Lebon, A., Marssi, E.M., Farhi, R., Dammak, H., Calvarin, G.: Translational and orientational order in lead zinc niobate: an optical and Raman study. *J. Appl. Phys.* **89**, 3947–3954 (2001)
63. R. Palai, Schmid, Hans, J. F. Scott, R. S. Katiyar, Raman spectroscopy of single-domain multiferroic BiFeO₃, *Phys. Rev. B* **81**, 064110–7(2010)
64. L. F. Cotica, V. F. Freitas, O. A. Protzek, J. A. Eiras, Garcia, F. Yokaichiya, I. A. Santos, R. Guo, and A. S. Bhalla, Tuning ferroic states in La doped BiFeO₃–PbTiO₃ displacive multiferroic compounds, *J. appl. phy.* **116**, 034107–6 (2014)
65. Eibschutz, M., Shtrikman, S., Treves, D.: Mossbauer studies of Fe⁵⁷ in Orthoferrites. *Phys. Rev. B.* **156**, 562–577 (1967)
66. James F. Scott, Ratnakar Palai, Ashok Kumar, Manoj K. Singh, Nishit M. Murari, Naba K. Karan, and Ram S. Katiyar, New Phase Transitions in Perovskite Oxides: BiFeO₃, SrSnO₃, and Pb(Fe_{2/3}W_{1/3})_{1/2}Ti_{1/2}O₃, *J. Am. Ceram. Soc.*, **91** [6] 1762–1768 (2008)
67. I. P. Raevski, S. P. Kubrin, S. I. Raevskaya, D. A. Sarychev, S. A. Prosandeev, and M. A. Malitskaya, Magnetic properties of PbFe_{1/2}Nb_{1/2}O₃: Mossbauer spectroscopy and first-principles calculations, *Phy. Rev. B* **85**, 224412–5 (2012)
68. Kuzian, R.O., Laguta, V.V., Richter, J.: Lieb-Mattis ferrimagnetic superstructure and superparamagnetism in Fe-based double perovskite multiferroics. *Phy. Rev.* **B90**, 134415–134417 (2014)
69. Jooy, P.A., Anil Kumar, P.S., Date, S.K.: The relationship between field-cooled and zero-field-cooled susceptibilities of some ordered magnetic systems. *J. Phys. Condens. Matter.* **10**, 11049–11054 (1998)
70. Laguta, V.V.: Superspin glass phase and hierarchy of interactions in multiferroic PbFe_{1/2}Sb_{1/2}O₃: an analog of ferroelectric relaxors? *New J. Phys.* **16**, 113041–113019 (2014)
71. Yang, J., Tong, W., Liu, Z., Zhu, X.B., Dai, J.M., Song, W.H., Yang, Z.R., Sun, Y.P.: Structural, magnetic, and EPR studies of the Aurivillius phase Bi₆Fe₂Ti₃O₁₈ and Bi₆FeCrTi₃O₁₈. *Phy. Rev. B.* **86**, 104410–104417 (2012)
72. Feng Yan, Guozhong Xing, Rongming Wang & Lin Li, Tailoring surface phase transition and magnetic behaviors in BiFeO₃ via doping engineering, *sci. rep.* **5**: 9128, 1–7 (2015)
73. A. Shengelaya, Guo-meng Zhao, H. Keller, and K. A. Muller, B. I. Kochelaev, EPR in La_{1-x}Ca_xMnO_{3+y}: relaxation and bottleneck, *Phy. Rev. B* **61**, 5888–5890 (2000)
74. Janhavi, P., Joshi, R.G., Sood, A.K., Bhat, S.V., Raju, A.R., Rao, C.N.R.: Temperature-dependent electron paramagnetic resonance studies of charge-ordered Nd_{0.5}Ca_{0.5}MnO₃. *Phy. Rev. B.* **65**, 024410–024418 (2001)
75. Bateni, A., Repp, S., Thomann, R., Selcuk Acar, E.E., Somer, M.: Defect structure of ultrafine MgB₂ nanoparticles. *App. Phys. Lett.* **105**(202605–4), 202605 (2014)
76. F. Menil. Systematic trends of the ⁵⁷Fe Mössbauer isomer shifts in (FeO) and (FeFn) polyhedra. Evidence of a New Correlation Between the Isomer Shift and the Inductive Effect of The Competing Bond T-X (*Fe) (Where X is O or F and T Any Element with a Formal Positive Charge). *J. Phys. Chem. Solids*, **46**, 763–789 (1985)
77. Pavlenko, A.V., Kubrin, S.P., Kozakov, A.T., Shilkina, L.A., Reznichenko, L.A., Nikolskii, A.V., Stashenko, V.V., Rusalev, Y.V., Petrosyan, K.S.: Phase transitions, dielectric, magnetic properties and valence of ions in AFe_{2/3}W_{1/3}O_{3±σ} (a = Ba, Sr) multiferroic ceramics. *J. Alloys Compd.* **740**, 1037–1045 (2018)
78. Raevski, I.P., Kubrin, S.P., Raevskaya, S.I., Titov, V.V., Sarychev, D.A., Malitskaya, M.A., Zakharchenko, I.N., Prosandeev, S.A.: Experimental evidence of the crucial role of nonmagnetic Pb

- cations in the enhancement of the Néel temperature in perovskite $\text{Pb}_{1-x}\text{Ba}_x\text{Fe}_{1/2}\text{Nb}_{1/2}\text{O}_3$. *Phy. Rev. B*. **80**, 024108–024106 (2009)
79. I. P. Raevski, V. V. Titov, M. A. Malitskaya, E. V. Eremin, S. P. Kubrin, A. V. Blazhevich, H. Chen, C. C. Chou, S. I. Raevskaya, I. N. Zakharchenko, D. A. Sarychev, S. I. Shevtsova. Studies of ferroelectric and magnetic phase transitions in multiferroic $\text{PbFe}_{0.5}\text{Ta}_{0.5}\text{O}_3$ – PbTiO_3 solid solution ceramics. *J. Mater. Sci.* **49**, 6459–6466 (2014)
80. J.B. Goodenough, *Magnetism and chemical bond*, Interscience Publisher (a division of Hohn Wiley & Sons), New-York – London, 393 (1963)

Publisher's note Springer Nature remains neutral with regard to jurisdictional claims in published maps and institutional affiliations.